



Available online at www.sciencedirect.com

ScienceDirect

Procedia Manufacturing 53 (2021) 656-663



www.elsevier.com/locate/procedia

49th SME North American Manufacturing Research Conference, NAMRC 49, Ohio, USA

Comparison of Early Stopping Neural Network and Random Forest for In-Situ Quality Prediction in Laser Based Additive Manufacturing

Matthew Behnke^a, Shenghan Guo^b, Weihong "Grace" Guo^{b,*}

^aDepartment of Computer Science, Colorado Mesa University, 1100 North Avenue, Grand Junction, CO 81501, USA ^bDepartment of Industrial and Systems Engineering, Rutgers, the State University of New Jersey, 96 Frelinghuysen Rd, Piscataway, NJ 08854, USA

* Corresponding author. Tel.: +1-848-445-8556; fax: +1-732-445-5467. E-mail address: wg152@soe.rutgers.edu

Abstract

Laser-Based Additive Manufacturing (LBAM) is a promising process in manufacturing that allows for capabilities in producing complex parts with multiple functionalities for a large array of engineering applications. Melt pool is a well-known characteristic of the LBAM process. Porosity defects, which have hampered the expansive adoption of LBAM, is correlated with the melt pool characteristic that occurs throughout the LBAM process. High-speed monitors that can capture the LBAM process have created the possibility for in-situ monitoring for defects and abnormalities. This paper focuses on augmenting knowledge of the relation between the LBAM process and porosity and providing models that could efficiently, accurately, and consistently predict defects and anomalies in-situ for the LBAM process. Two models are presented in this paper, Random Forest Classifier and Early Stopping Neural Network, which are used to classify pyrometer images and categorize if those images will result in defects. Both methods can achieve over 99% accuracy in an efficient manner, which would create an in-situ method for quality prediction in the LBAM process.

© 2021 The Authors. Published by Elsevier B.V.

This is an open access article under the CC BY-NC-ND license (http://creativecommons.org/licenses/by-nc-nd/4.0/) Peer-review under responsibility of the Scientific Committee of the NAMRI/SME

Keywords: Machine Learning; Laser Based Additive Manufacturing; Deep Learning; Random Forest

1. Introduction

The ability to produce complex and elaborate parts with additive manufacturing (AM) is desired in many fields. Laser-based additive manufacturing (LBAM) refers to a branch of AM processes that use a laser beam to provide the thermal energy for melting and consolidating the added material powders. One of the most representative LBAM processes is direct energy deposition (DED) [1]. DED has the potential to achieve such flexible, customized production. However, the quality of DED-produced parts is unstable. Porosity has been noted as a major defect, causing microstructure and stability issues [2]. The occurrence of porosity is closely related to abnormal thermal dynamics in melt pool during the DED process [3], but there are insufficient studies for accurately predicting the porosity in real time. These issues have prevented the wide-spread adoption of LBAM-produced parts.

This has prompted studies on porosity detection based on *in-situ thermal images* of melt pool. During a typical DED process, the material powder is injected by a nozzle onto the substrate, creating a melt pool. Recent improvements to sensing technology make it possible to capture real-time (in-situ), high-speed images for the melt pool throughout the

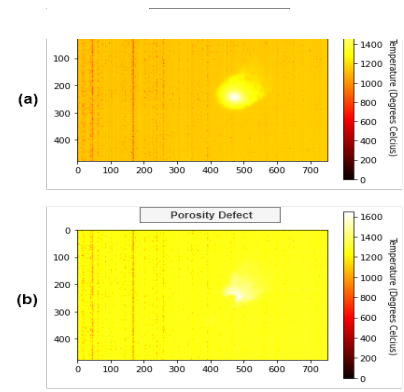


Fig. 1. An in-situ thermal image of melt pool from the DED process of a Ti-6Al-4V thin-walled part. (a) Shows a DED thermal image with no porosity defect. (b) Shows a DED thermal image with a porosity defect.

manufacturing process. Fig. 1 shows two examples of the insitu thermal images of melt pool from the DED process of a Ti-6Al-4V thin-walled part. Each pixel in Fig 1. represents a value in a degree Celsius. The heat-affected zone on the middle-right of the image is melt pool. It is hotter than the surrounding area. The highest temperature (i.e., brightest color) is observed in the centre of melt pool.

In-situ thermal images of melt pool are evidence for identifying porosity. Literature [4] has shown that porosity is closely related to the abnormal thermal dynamics in melt pool. Khanzadeh et al. proposed two types of tensor decomposition models, T^2 chart and Q chart, to predict porosity, as well as a KNN to predict porosity levels during the DED process [2, 3]. Tootooni et al. [5] applied a group of classifiers to the Laplacian eigenvalues extracted from 3D cloud data to detect dimension variation. Neural Networks (NNs) were adopted in Lu et al. [6], Caiazzo and Caggiano [7], Xiong et al. [8] to predict part geometry in AM. The prediction in turn became the evidence for optimizing the process parameters in DED. Random Forest (RF) was trained with CT scanning/thermal images for porosity prediction in Ren and Mazumder [9], and for surface defect prediction in Li et al. [10] and Chen et al. [11]. A semi-supervised methods, which consisted of feature extraction from large imaging data and randomized singular value decomposition. was used in Okaro et al. [12] for fault detection in LBAM processes. These studies have had success and trailblazed the way for successful methodology in predicting part defects such as porosity or geometric variation. However, despite their remarkable methodological contribution, improvement can still be made in using ML methods to predict porosity.

The contribution of this work is to propose an integrated method for accurate in-situ prediction of porosity in DED. Fig. 2 demonstrates the structure of our method. Two robust, accurate, and time-efficient models, namely RF and Early Stopping Neural Network (ESSN), are used along with three innovative ways of image pre-processing (i.e., manual visualization-based crop, automated heat-based crop, Principal Component Analysis (PCA) crop) to improve the prediction accuracy. The case study shows that the proposed method consistently achieved prediction accuracies over 99%, which has defeated benchmark studies based on the same dataset. A thorough evaluation of the prediction power against porosity is provided by the misclassification rate in individual deposition layers.

In RF, multiple tree predictors are built independently, with each tree underlaid by a bootstrapped sample (independently sampled) from the training data. These tree predictors are aggregated to reduce the bias of individual tree and increase the robustness of prediction. The error from RF depends on the strength of the individual trees in the forest and the correlation between them [13]. One advantage that ESSN has over the RF model, is that RF requires another step of preprocessing before data can be trained or predicted on. Pyrometer images must first be flattened into a vector from a matrix before use, while ESSN does not have to do this. ESSN may also perform faster in certain scenarios. Many deep learning libraries, like Google's Tensorflow, now have the ability to train on Graphics Processing Units (GPUs) or Tensor Processing Units (TPU) which greatly speed up training and prediction. This could create neural networks that perform faster than RF.

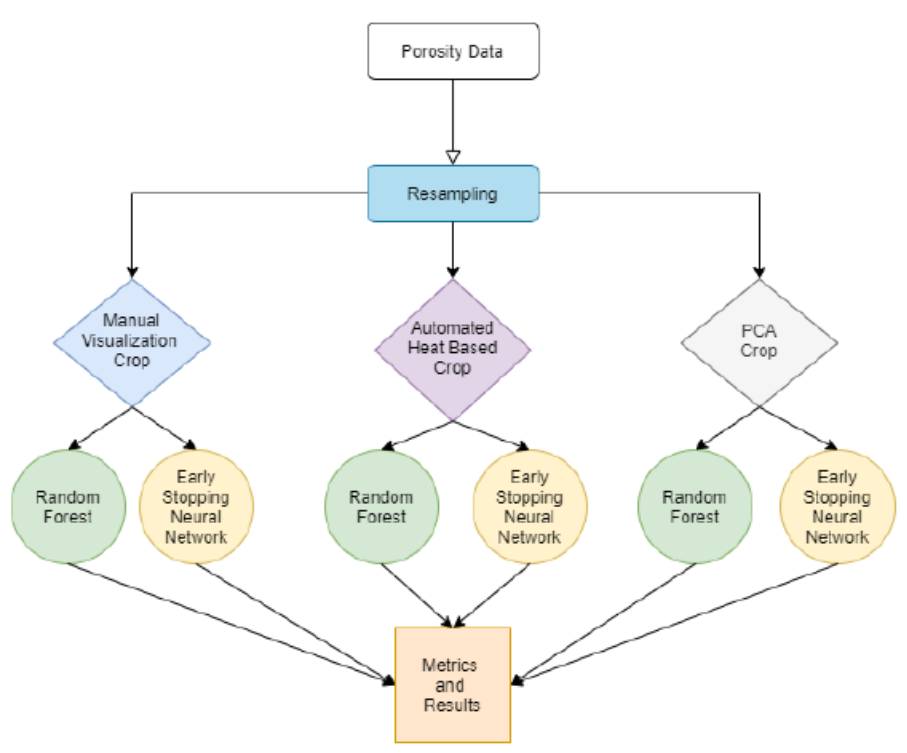


Fig. 2. Structure of the proposed method.

The rest of this paper is organized as follows. Section 2 will explain the data collection and label (i.e., porosity occurrence) assignment. Section 3 will describe data preprocessing. Multiple ways are introduced for reducing redundant information and balancing the instances related/not related to porosity occurrence. Section 4 will provide the methodology details for the proposed models, i.e., RF and ESNN. Section 5 will provide case study results and discuss the performance of both models. The paper is concluded by Section 6.

Nomenclature

x, y
 Row and column index of pixel in a thermal image
 x*, y*
 Central pixel location of melt pool
 N
 Number of thermal images associated with porosity
 T
 Number of decision trees in Random Forest
 J
 Index of resampled image in bootstrap
 U
 A computer-generated random number following

Uniform(0, 1) distribution

2. Data Description

This section will introduce the dataset motivating this study. Data collection of in-situ thermal images (Section 2.1) and porosity records (Section 2.2) are both elaborated. These data will be underlying the case study in Section 5.

2.1. Data Collection

This study is based on in-situ thermal images from a DED process of Ti-6Al-4V thin-walled part (referred as "DED dataset" in the following context). The data were first introduced in Marshall *et al.* [14] and then became a benchmark dataset for DED studies. Laser Engineered Net Shaping (LENSTM) 750 system was the equipment for manufacturing the thin-walled part. An inline pyrometer collected thermal images of melt pool in real time at a nominal collection rate of 6.4Hz and a temperature range of [1000°C, 2500°C]. The pyrometer produces thermal images in the form of Comma Separated Values (CSV) files. Each CSV file corresponds to one thermal image and contains a pixel matrix of size 752 × 480.

2.2. Porosity Records

Each thermal image (CSV file) is associated with a porosity record that indicates the size of pores (in millimeter or mm) in part at the time of image collection. These porosity labels are measured offline and manually by 3D computerized tomography (CT) scanning for the finished thin-walled part. The image collection time corresponds to the location to be scanned in part. A thermal image associated with pores over 0.05mm is related to porosity occurrence and thus considered "bad". Otherwise it is "good". The entire dataset consisted of 1486 'good' samples and 70 'bad' samples.

3. Data Preprocessing

This section proposes effective data preprocessing for the thermal imaging data to facilitate porosity prediction. Resampling is first discussed in Section 3.1 as means to overcome the imbalance between "good" and "bad" samples. Three ways of cropping thermal images are introduced in Section 3.2 to reduce irrelevant information in data, which are manual visualization-based crop (subsection 3.2.1), automated melt pool crop (subsection 3.2.2), and PCA-based crop (subsection 3.2.3), respectively.

3.1. Resampling

To train a machine learning model that accurately classifies "good" and "bad" thermal images, there should be a good balance between the two types of instances in the training data. However, data from real applications can be heavily imbalanced. For example, the "good" instances in DED dataset outnumbered the "bad" ones by 1486 to 70. Such imbalance can compromise the validity and accuracy of the model. There is a motivation to make the data balanced by equalizing the number of "good" and "bad" instances with bootstrap resampling [15].

In bootstrap, the N original "bad" instances are indexed from 0 to N. An index (J) is selected randomly as

$$I = |UN| + 1 \tag{1}$$

where $U \sim \text{Uniform}(0, 1)$ is a computer-generated random number and $[\cdot]$ is the floor of the value. Then the Jth "bad" thermal image is selected and appended to the original set of N "bad" instances. This bootstrap process continues until the number of "bad" instances, including the resampled ones, accumulate to an equal value with the "good" instances. For the DED dataset, bootstrap resulted in 1486 "bad" instances. With the 1486 "good" ones, there are 2972 instances in total.

3.2. Thermal Image Cropping

One critical issue with raw thermal images (see Fig. 1) is the inclusion of a large background. The background is irrelevant to melt pool and may contain noisy IR radiation. It elevates the computational burden in data processing and may compromise the accuracy of porosity prediction. The solution to this problem is *image cropping*, which preserves the image segments relevant to the melt pool and eliminates redundant information. Three types of cropping methods are introduced in this section (see Fig. 3) and then applied to the DED dataset in case study (Section 5).

3.2.1. Manual visualization-based cropping

This is a direct crop of the thermal image based on visual estimation of the melt pool location. For the DED dataset, preliminary image visualization shows that the melt pool location is relatively stable. Let x be the row index (increases from top to bottom) and y be the column index (increases from left to right) of a pixel, then a visual estimate of the melt pool location is $x \in [350, 600], y \in [90, 340]$. Fig. 4 shows the boundaries from visualization-based crop on a raw

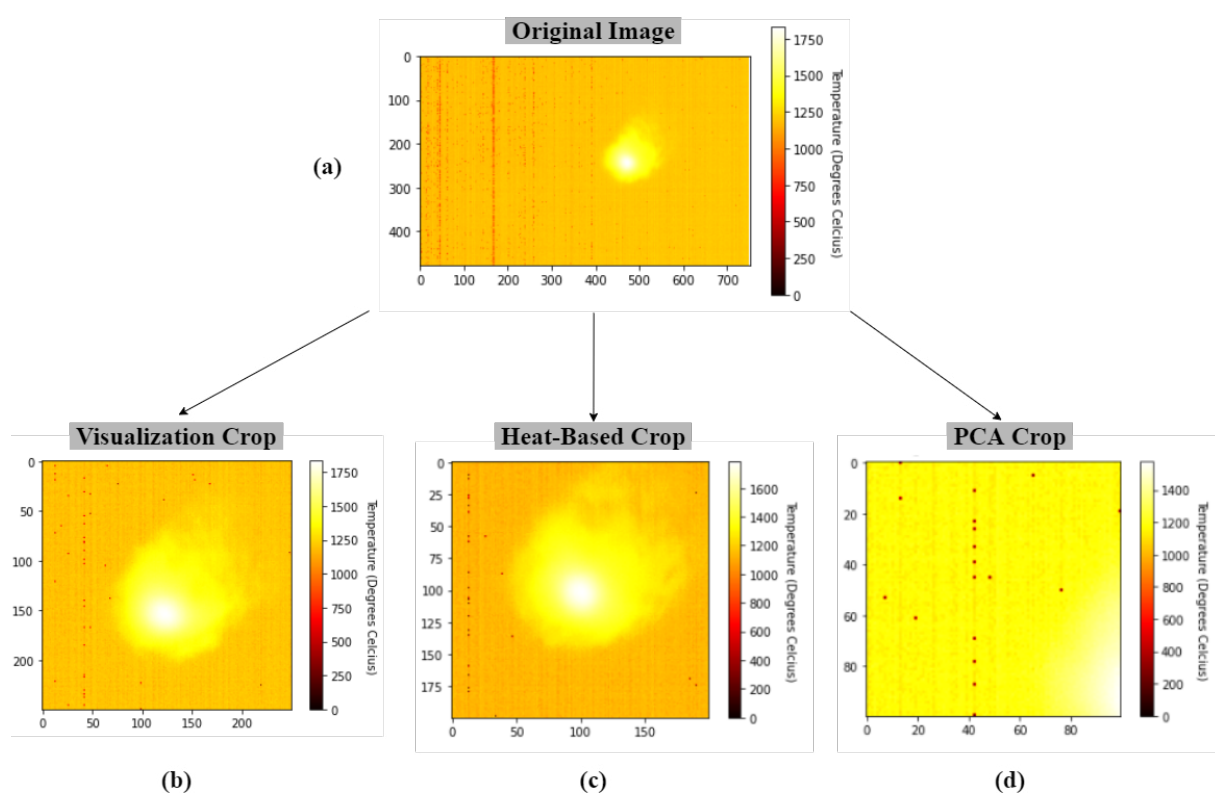


Fig. 3. Data pre-processing: (a) Sample of an original image captured via pyrometer, (b) image after manual visualization-based crop, (c) image after heat-based crop, and (d) image after PCA-based crop.

thermal image from the DED dataset. The large background was effectively reduced.

3.2.2. Automated heat-based cropping

This cropping method finds the hottest pixel in a thermal image and makes that pixel the image centre, (x^*, y^*) . The melt pool location is estimated as the surrounding square matrix of certain size, e.g., 250×250 in the DED dataset. Specifically, the 125 rows above and below x^* plus the 125 columns to the left and right of y^* should be taken as the melt pool crop. Fig. 3(c) shows an example of the melt pool image after automated heat-based cropping.

To find (x^*, y^*) , a greedy search for the highest pixel value is done for each image. If more than one pixel is tied for the highest temperature in an image, then the (x, y) coordinates of the hottest pixels are averaged out to create one coordinate. The non-integer values of (x, y) are rounded to the nearest integer. This cropping scheme is "automated" in the sense that the estimated melt pool location is adapted from the image and obtained automatically rather than manually assigned. Provides an example of a melt pool crop produced by this scheme. It is close to the result of manual visualization-based crop. The melt pool was well preserved while the irrelevant background was removed.

3.2.3. PCA-based cropping

PCA is a feature extraction method that extracts critical features in the form of *principal components (PCs)* from the data [16]. Unimportant information (features) is eliminated,

which leads to its key merits – data denoise and dimensionality reduction [17, 18].

For a thermal image, PCA is used to extract a number of PCs that are associated with the major portion of pixel-wise variance. It has been observed in Fig. 1 that the pixel-wise variance, or temperature variation, in a raw thermal image mainly occur in the region of melt pool. So, the pixels

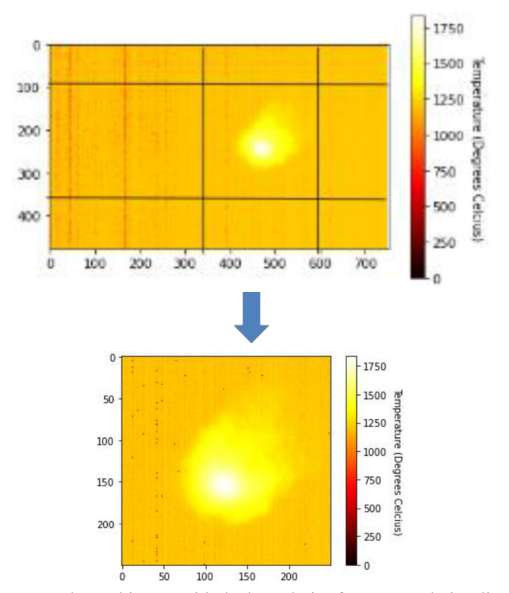


Fig. 4. A raw thermal image with the boundaries from manual visualizationbased crop (top) and the corresponding melt pool crop (bottom).

forming these PCs are very likely to be those in the melt pool regions. Image cropping should be done based on these pixels' coordinates.

To use PCA on DED dataset, first the pixel matrix is vectorized, then fed to the PCA library from "scikit-learn" package. After the model fitting, the M PCs that explain 95% data variance (or variability ratio) are picked. A new PCA model with these PCs is fit, which creates a list of every feature marked by its importance (i.e., magnitude of eigenvalue). The top 10 biggest eigenvalues are selected from each component. For each eigenvalue list for every component, if there is a singular mode in either x or y coordinate, the value is saved; otherwise, the average of those 10 coordinates were used. Then for all M components, the mode of x and y coordinates are taken to form the center (x^*, y^*) . If there is no singular mode, the average of either x or y coordinate is selected to form (x^*, y^*) . A 100×100 pixel matrix is created around (x^*, y^*) . Fig. 3(d) shows a melt pool cropped with the PCA method. Compared to manual visualization-based crop and automated melt pool crop, this scheme has led to certain loss of melt pool, but this can be improved by taking larger than 10 eigenvalues from the 2nd PCA model to identify the melt pool center.

4. Method

In this section, we introduce the models for porosity prediction, namely RF (Section 4.1) and ESNN (Section 4.2).

4.1. Random Forest

RF is an ensemble learning method that is extensively used in image classification for their remarkable classification accuracy [19, 20]. An RF model aggregates a number (T) of decision trees. For the DED dataset, T=10 is adopted and data is vectorized before model training. In a single decision tree, an instance is classified by going through a sequence of node. A node is equivalent to a binary (0 or 1) decision that determines the direction the instance should go for the next step (subsequent node). A "tree"

structure is essentially formed by a sequence of binary decisions, thus the name "decision tree". By aggregating (averaging) the classification results of *T* decision trees, an RF model can increase the decision's robustness and reduce the bias.

4.2. Proposed Early Stopping Neural Network (ESNN)

Convolutional Neural Network (CNN) is a trending model for efficient and accurate classification of imaging data. This has been exemplified through larger datasets, e.g., ImageNet, whose classification performance is featured by low error rates and high accuracy [21, 22]. We develop ESNN based on CNN that stop model training early to prevent overfitting. The architecture of ESNN is demonstrated in Fig. 5. The input are individual thermal images with shape $250 \times 250,200 \times 200$, or 100×100 (i.e., height×width, and depth = 1). The cropping method is any one of the three proposed schemes: manual visualization-based crop, automated heat-based crop, or PCA-based crop. The cropped image goes through several convolutional blocks that are designed to extract features from the image. Here, the "features" are the outcome of applying image convolution.

The first four blocks of ESNN each consists of a 2D convolutional layer (Conv2D), a Max Pooling layer, and a Batch Normalization layer. Similar to the use of Conv2D in the Very Deep Convolutional Neural Network for Large-Scale Image Recognition [23], the Conv2D layer uses a 3×3 kernel captures the essence of up, down, left, in the smallest way possible for the images. The filter size, which is the parameter that is used to extract features from the images, is determined per the convention of CNN classification for 224×224 images, so are the rest ESNN parameters. All the Conv2D layers in ESNN are followed by Max Pooling layers. The function of Max Pooling layers is to perform spatial pooling, which groups features to those that are adjacent or in an approximate area to it.

The last four blocks of ESNN each consists of a Batch Normalization layer. This layer accelerates the training of

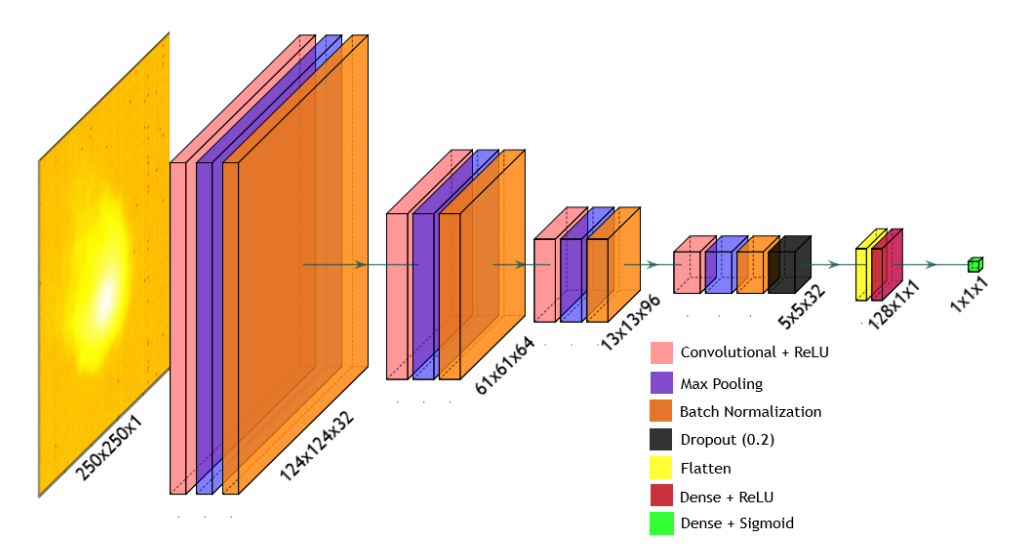


Fig. 5. Architecture for the proposed early stopping neural network (ESNN).

ESNN while allowing for higher training rates and accuracy [24]. After 4 blocks of the ESNN, the data encounters its first dropout layer. This layer is used in prevention of overfitting, as large neural networks by randomly dropping neurons from the network and their connections [25]. This methodology prevents overfitting by making sure that many neurons in the network do not have highly correlated behavior. Following the dropout layer, the Flatten layer converts the data into a vector which is required for the next fully connected dense layer. Finally, this is led into a dense layer with a sigmoid activation function which is used to transform the final input of the neural network into a value between 0 and 1. This is the final classification for the data, with "0" corresponds to a "good" instance and "1" corresponds to a "bad" one.

The model is compiled using the "Keras" package. Model training is fulfilled by adopting Stochastic Gradient Descent (SGD) as the optimizer, binary cross entropy as the loss function, and accuracy as the performance metric. Throughout model training, it was seen that the validation accuracy of the last epoch was highly correlated with the test accuracy. Hence, if the last epoch had a low validation accuracy, then the test accuracy would also suffer, but high validation accuracy scores resulted in desirable test accuracy scores. An early stopping call back method was employed to consistently result in a well-trained model. First, the number of epochs was set at a 50 and a patience value was set to 10. Patience value refers to the number of epochs a model will continue to train while a specified metric is not improving, in this case, the desired metric is validation accuracy. If the model exceeds the patience value before training is complete, it will revert to the epoch with the best validation accuracy. The last epoch will be variable depending on the data ESSN receives. This underlies the importance of setting a high number of epochs, because the model could plummet from a high validation accuracy in the penultimate epoch to a low validation accuracy in the final epoch, which results in a lowtest accuracy. If the model has a high number of epochs, it becomes increasingly more unlikely that the model will finish through all the epochs.

5. Results and Discussion

In this section, we elaborate porosity prediction with the trained ESNN, and define the accuracy measurements (Section 5.1). The prediction performance of RF and ESNN, based on varying cropping schemes, are compared (Section 5.2). The effect of different cropping methods is compared and discussed in Section 5.3. Finally, analysis of incorrect prediction is done for deposition layers in Section 5.4.

5.1. Testing Configuration and Accuracy Measurement

Both models were trained through various training and testing ratios to examine how the models would perform under different amounts of training data. For each split, the data is shuffled to see how both models perform with different sets of data and to avoid testing on the same consistent split. When either model predicts it can either produce a '0' or a '1'. In this case '0' will be viewed as 'positive' and '1' will be viewed as 'negative'. If either a '0'

or '1' is accurately predicted it is considered 'true'; otherwise, it would be considered as 'false'. Thus, the four classifications a prediction can have is: True Positive (TP), True Negative (TN), False Positive (FP), False Negative (FN). Test accuracy is defined in Eq. (2):

Test Accuracy (%) =
$$\frac{TP + TN}{TP + FP + TN + FN}$$
 (2)

For every training and testing split ratio there are 25 trials and the average of those accuracy scores is recorded as the average accuracy for both models. Time is also recorded, where time refers to the average amount of time it took for the model to train and predict a random split.

5.2. Performance Evaluation

From Table 1, we can see that both RF and ESNN achieved very high rates of accuracy for the manual visualization-based crop alone. Both models were able to achieve an average accuracy percentage above 99% in multiple training and testing ratios. The most notable discrepancy between RF and ESNN results was the 10% training and 90% testing ratio. The ESNN performed poorly on this set, with an average accuracy of 59.83%, which was slightly better than guessing. The RF model, however, performed well at this training and testing ratio, with 98%

Table 1. Performance in porosity prediction for the DED dataset using manual visualization-based crop.

	Test	Accuracy (%)	Time (sec)		
Training /Testing	Random	Early Stopping	Random	Early Stopping	
Split Ratio	Forest	Neural Network	Forest	Neural Network	
10/90	98.45	59.83	2.49	12.02	
20/80	99.26	94.66	4.30	31.58	
30/70	99.67	98.19	6.18	37.02	
40/60	99.68	99.18	7.82	43.39	
50/50	99.57	99.00	9.56	50.98	
60/40	99.82	99.69	11.37	60.78	
70/30	99.79	99.50	13.07	72.20	
80/20	99.75	99.90	14.66	75.84	

Table 2. Performance in porosity prediction for the DED dataset using automated heat-based crop.

	Test	Accuracy (%)	Time (sec)		
Training /Testing	Random	Early Stopping	Random	Early Stopping	
Split Ratio	Forest	Neural Network	Forest	Neural Network	
10/90	96.48	66.23	2.20	10.12	
20/80	99.14	98.56	3.95	21.89	
30/70	99.58	98.08	5.71	29.14	
40/60	99.84	99.01	12.17	31.69	
50/50	99.46	96.29	10.09	15.21	
60/40	99.64	99.49	12.00	22.18	
70/30	99.78	99.72	13.80	24.05	
80/20	99.90	99.53	15.55	25.63	

Table 3. Performance in porosity prediction for the DED dataset using PCA-based crop.

	Test Accuracy (%)		Time (sec)		
Training /Testing Split Ratio	Random Forest	Early Stopping Neural Network	Random Forest	Early Stopping Neural Network	
10/90	95.46	49.63	0.80	4.13	
20/80	97.88	62.00	1.57	6.86	
30/70	98.80	93.64	2.25	11.98	
40/60	99.04	99.43	2.95	23.99	
50/50	99.46	98.25	3.53	34.46	
60/40	99.64	99.70	4.19	43.71	
70/30	99.78	99.81	4.75	48.02	
80/20	99.91	99.13	5.46	47.79	

accuracy. These results show that the ESNN performs worse when compared to the RF model when given lower ratios of training data, but when given around an even 50/50 split, they perform at equal levels.

In Table 2, the results of the automated melt pool crop can be seen for both models. In this table with this style of cropping method, that test accuracy scores for both the RF and ESNN score very well. For RF, all training ratios above 10% scored an average accuracy above 99% and for the ESNN it consistently scored an average accuracy score above 99% above the 50% training ratio.

In Table 3, the metrics for automated PCA Crop can be seen. For RF, the accuracy was consistently over 99% average accuracy score above the 30% training ratio. The ESNN consistently achieved an average accuracy above 99% above 50% training ratio, similar to the melt pool automated crop. The time for both the RF and ESNN were significantly decreased compared to both the manual visualization crop and the melt pool automated crop, mainly due to the crop size being 100×100 in comparison to 200×200 and 250×250 .

5.3. Comparison of Cropping Methods

In a direct comparison of all three different types of cropping styles in Table 4 and Table 5, all three of the methodologies have high test accuracies scores. All three cropping methods received a test accuracy score above 99% in training ratios 60% and above. In terms of time, the PCA-based crop trained and predicted in the shortest amount of time as it only had to train on images 100×100 (width×height). The automated heat-based crop also was faster than the manual visualization-based crop as it was 200×200 compared to 250×250 (width×height).

For which method should be used for in- situ monitoring, despite all three achieving similar metrics, the automated heat-based crop provides the most robust algorithm of the three for in-situ monitoring. The manual visualization-based crop and PCA based crop, provided a relatively static method where the same crop was applied to the entire dataset, which worked solely in terms of this dataset. During the DED process, the melt pool may be located in various areas, which eliminates the possibility of a static crop. With the automated heat-based crop, the image would automatically focus in on the melt pool which would be a necessary feature for in-situ quality prediction, especially over many different DED processes.

5.4. Performance by Deposition Layer

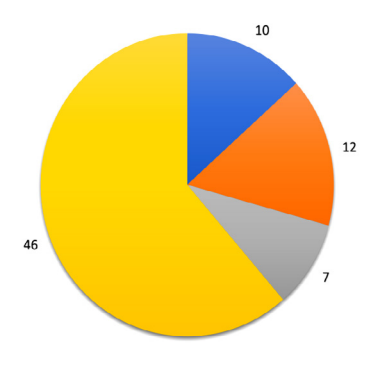
To test which layers during the DED process are misidentified most often by our models, a 50/50 train/test split with the ESNN model was deployed with false positive and false negatives categorized by layer are displayed in Fig 6. In Fig. 6, layers 1, 2, and 3 accounts for 38.66% of the total incorrectly classified data during the prediction process, despite only accounting for 5% of the total layers. Layers 4-60, at most had accumulative incorrect predictions of 2 or below. It is believed that this could be due the nature of the DED process. When metallic powder is first laid into the machine, the plate is much cooler since no melting has occurred yet. This may cause the incorrect predictions since

Table 4. Comparison of cropping methods with RF.

	Test Accuracy (%)			Ti	Time (sec)		
Training	Manual	Automated	PCA-	Manual	Automated	PCA-	
/Testing	Visualization-	Heat-	based	Visualization-	Heat-	based	
Split	Based Crop	Based	Crop	Based Crop	Based	Crop	
Ratio		Crop			Crop		
10/90	98.45	96.48	95.46	2.49	2.20	0.80	
20/80	99.26	99.14	97.88	4.30	3.95	1.57	
30/70	99.67	99.58	98.80	6.18	5.71	2.25	
40/60	99.68	99.84	99.04	7.82	12.17	2.95	
50/50	99.57	99.46	99.46	9.56	10.09	3.53	
60/40	99.82	99.64	99.64	11.37	12.00	4.19	
70/30	99.79	99.78	99.78	13.07	13.80	4.75	
80/20	99.75	99.90	99.91	14.66	15.55	5.46	

Table 5. Comparison of cropping methods with ESNN.

	Test Accuracy (%)			Ti	Time (sec)		
Training	Manual	Automated	PCA-	Manual	Automated	PCA-	
/Testing	Visualization-	Heat-	based	Visualization-	Heat-	based	
Split	Based Crop	Based	Crop	Based Crop	Based	Crop	
Ratio		Crop			Crop		
10/90	59.83	66.23	49.63	12.02	10.12	4.13	
20/80	94.66	98.56	62.00	31.58	21.89	6.86	
30/70	98.16	98.08	93.64	37.02	29.14	11.98	
40/60	99.18	99.01	99.43	43.39	31.69	23.99	
50/50	99.00	96.29	98.25	50.98	15.21	34.36	
60/40	99.69	99.49	99.70	60.78	22.18	43.71	
70/30	99.50	99.72	99.81	72.20	24.05	48.02	
80/20	99.90	99.53	99.13	75.84	25.63	47.79	



■Layer 1 ■Layer 2 ■Layer 3 ■Layer 4-60

Fig. 6. Pie chart depicting the number of incorrectly classified images by ESNN based on deposition layer.

these layers specifically have another underlying process if heating up, compared to later layers.

6. Conclusion

In this paper, RF and ESNN were proposed for in-situ quality prediction precision in DED. These models use pyrometer images to detect porosity levels and make a quality prediction of the part. The results demonstrate that both methods have a high level of accuracy, efficiency, and consistency, which proves that this method can be used for in-situ porosity detection in the DED process. This study also gives indication as to which layers may be predicted incorrectly more than others because of the nature of the DED process. These promising results in achieving accurate predictions for quality prediction during the DED process could also create future work in isolating which areas of pyrometer images cause the porosity defects. Future work may also include further research of ESSN into creating an optimal stopping algorithm for model training and how ESSN performs on other DED or additive manufacturing datasets.

Acknowledgements

The authors would like to thank the Center for Discrete Mathematics and Theoretical Computer Science (DIMACS) at Rutgers University for providing research experience under the National Science Foundation (NSF)-sponsored DIMACS Research Experiences for Undergraduates (REU) program (grant CCF-1852215). The authors would also like to thank Prof. Linkan Bian's team for providing the case study data and domain knowledge.

References

- Gibson, I., Rosen, D.W., Stucker, B., 2014, Additive manufacturing technologies, 2nd ed., Springer.
- [2] Khanzadeh, M., Tian, W., Yadollahi, A., Doude, H.R., Tschopp, M.A., Bian, L., 2018, Dual process monitoring of metal-based additive manufacturing using tensor decomposition of thermal image streams, Additive Manufacturing, 23: 443-456.
- [3] Khanzadeh, M., Chowdhury, S., Marufuzzaman, M., Tschopp, M.A., Bian, L., 2018, Porosity prediction: Supervised-learning of thermal history for direct laser deposition, Journal of Manufacturing Systems, 47: 69-82
- [4] Seifi, S.H., Tian, W., Doude, H., Tschopp, M.A., Bian, L., 2019, Layer-Wise Modeling and Anomaly Detection for Laser-Based Additive Manufacturing, Journal of Manufacturing Science and Engineering, 141(8).
- [5] Tootooni, M.S., Dsouza, A., Donovan, R., Rao, P.K., Kong, Z.J., Borgesen, P., 2017, Classifying the Dimensional Variation in Additive Manufactured Parts from Laser-Scanned Three-Dimensional Point Cloud Data Using Machine Learning Approaches, Journal of Manufacturing Science and Engineering, Transactions of the ASME, 139(9)
- [6] Lu, Z.L., Li, D.C., Lu, B.H., Zhang, A.F., Zhu, G.X., Pi, G., 2010, The prediction of the building precision in the Laser Engineered Net Shaping process using advanced networks, Optics and Lasers in Engineering, 48(5): 519-525.
- [7] Caiazzo, F., Caggiano, A., 2018, Laser Direct Metal Deposition of 2024 Al Alloy: Trace Geometry Prediction via Machine Learning, Materials. 11(3): 444.
- [8] Xiong, J., Zhang, G., Hu, J., Wu, L., 2014, Bead geometry prediction for robotic GMAW-based rapid manufacturing through a neural network and a second-order regression analysis, Journal of Intelligent Manufacturing, 25(1): 157-163.
- [9] Ren, W., Mazumder, J., 2020, In-situ porosity recognition for laser additive manufacturing of 7075-Al alloy using plasma emission spectroscopy, Scientific Reports, 10(1): 19493.

- [10] Li, Z., Zhang, Z., Shi, J., Wu, D., 2019, Prediction of surface roughness in extrusion-based additive manufacturing with machine learning, Robotics and Computer-Integrated Manufacturing, 57: 488-495
- [11] Chen, L., Yao, X., Xu, P., Moon, S.K., Bi, G., 2021, Rapid surface defect identification for additive manufacturing with in-situ point cloud processing and machine learning, Virtual and Physical Prototyping, 16(1): 50-67.
- [12] Okaro, I.A., Jayasinghe, S., Sutcliffe, C., Black, K., Paoletti, P., Green, P.L., 2018, Automatic Fault Detection for Selective Laser Melting using Semi-Supervised Machine Learning.
- [13] Breiman, L., 2001, Random Forests, Machine Learning, 45(1): 5-32.
- [14] Marshall, G.J., Thompson, S.M., Shamsaei, N., 2016, Data indicating temperature response of Ti-6Al-4V thin-walled structure during its additive manufacture via Laser Engineered Net Shaping, Data in brief, 7: 697-703.
- [15] Rubinstein, R.Y., Kroese, D.P., 2016, Simulation and the Monte Carlo method, John Wiley & Sons.
- [16] Abdi, H., Williams, L.J., 2010, Principal component analysis, Wiley interdisciplinary reviews: computational statistics, 2(4): 433-459.
- [17]Zhang, L., Dong, W., Zhang, D., Shi, G., 2010, Two-stage image denoising by principal component analysis with local pixel grouping, Pattern Recognition, 43(4): 1531-1549.
- [18] Mudrova, M., Procházka, A., Principal component analysis in image processing, in: Proceedings of the MATLAB Technical Computing Conference, Prague, 2005.
- [19] Millard, K., Richardson, M., 2015, On the importance of training data sample selection in random forest image classification: A case study in peatland ecosystem mapping, Remote sensing, 7(7): 8489-8515.
- [20] Du, P., Samat, A., Waske, B., Liu, S., Li, Z., 2015, Random Forest and Rotation Forest for fully polarized SAR image classification using polarimetric and spatial features, ISPRS Journal of Photogrammetry and Remote Sensing, 105: 38-53.
- [21] Yoo, C., Han, D., Im, J., Bechtel, B., 2019, Comparison between convolutional neural networks and random forest for local climate zone classification in mega urban areas using Landsat images, ISPRS Journal of Photogrammetry and Remote Sensing, 157: 155-170.
- [22] Krizhevsky, A., Sutskever, I., Hinton, G.E., 2017, Imagenet classification with deep convolutional neural networks, Communications of the ACM, 60(6): 84-90.
- [23] Simonyan, K., Zisserman, A., 2014, Very deep convolutional networks for large-scale image recognition, arXiv preprint arXiv:1409.1556.
- [24] Ioffe, S., Szegedy, C., 2015, Batch normalization: Accelerating deep network training by reducing internal covariate shift, arXiv preprint arXiv:1502.03167.
- [25] Srivastava, N., Hinton, G., Krizhevsky, A., Sutskever, I., Salakhutdinov, R., 2014, Dropout: a simple way to prevent neural networks from overfitting, The journal of machine learning research, 15(1): 1929-1958.